

# Computation of the Beavers–Joseph slip coefficient for coupled Stokes/Darcy problems

Paula Strohbeck, Elissa Eggenweiler, Iryna Rybak

*University of Stuttgart, Institute of Applied Analysis and Numerical Simulation,  
Pfaffenwaldring 57, 70569 Stuttgart, Germany*

---

## Abstract

Physically consistent coupling conditions at the fluid–porous interface with correctly determined effective parameters are necessary for accurate mathematical modeling of various applications described by coupled free-flow and porous-medium problems. To model single-fluid-phase flows at low Reynolds numbers in such coupled systems, the Stokes/Darcy equations are typically used together with the conservation of mass across the fluid–porous interface, the balance of normal forces and the Beavers–Joseph condition on the tangential component of velocity. In the latter condition, the value of the Beavers–Joseph slip coefficient  $\alpha_{\text{BJ}}$  is uncertain, however, it is routinely set  $\alpha_{\text{BJ}} = 1$  that is not correct for many applications. In this paper, three flow problems (pressure-driven flow, lid-driven cavity over porous bed, general filtration problem) with different pore geometries are studied. We determine the optimal value of the Beavers–Joseph parameter for unidirectional flows minimizing the error between the pore-scale resolved and macroscale simulation results. We demonstrate that the Beavers–Joseph slip coefficient is not constant along the fluid–porous interface for arbitrary flow directions, thus, the Beavers–Joseph condition is not applicable in this case.

*Keywords:* Stokes equations, Darcy’s law, interface conditions, Beavers–Joseph parameter

*2010 MSC:* 65K10, 65N08, 76D07, 76S05

---

## 1. Introduction

Coupled porous-medium and free-flow systems appear in a variety of environmental and technical applications such as interaction between surface and

subsurface water, geothermal problems and industrial filtration processes [1–3]. From the macroscale perspective, fluid flow in the free-flow domain and through the porous medium is described by two different sets of equations, which need to be coupled at the fluid–porous interface [4–8]. Fluid flows through such coupled systems are highly interface driven, therefore, the correct choice of coupling conditions and effective model parameters is crucial for accurate numerical simulation of applications.

Depending on the flow problem, different mathematical models and different sets of coupling conditions at the fluid–porous interface exist, e.g., [4, 6, 7, 9–13]. Most often, the Navier–Stokes equations or, in case of low Reynolds numbers, the Stokes equations are used to describe the fluid flow in the free-flow region while in the porous-medium domain Darcy’s law or one of its generalizations is applied. Besides the Stokes equations, there are several other simplifications of the Navier–Stokes equations, which can be used to model surface flows, such as the shallow water equations, kinematic or diffusive wave equations [9, 11, 14]. For higher Reynolds numbers, the Forchheimer equation is used in the porous medium and coupled to the free-flow model [2, 4]. To describe two-fluid-phase flows in the subsurface, the Richards equation or two-phase Darcy’s law is applied [1, 15, 16].

Based on the choice of the underlying flow models in the free-flow region and the porous medium, different sets of coupling conditions at the fluid–porous interface are available in the literature. Interface conditions for the Navier–Stokes/Darcy–Forchheimer model are developed in [2, 17–19]. Coupling conditions for the Stokes equations and multiphase Darcy’s law together with the transport of chemical species and energy are proposed in [15]. Coupling strategies for the Stokes/Darcy–Brinkman equations are derived in [4]. The most widely studied problem in the literature, both from the modeling and numerical point of view, is the Stokes/Darcy problem describing single-fluid-phase flows in coupled free-flow and porous-medium systems. For this model, different coupling strategies exist, e.g., [4, 7, 8, 20–22]. However, the classical set of coupling conditions, which comprises the conservation of mass across the interface, the balance of normal forces and the Beavers–Joseph condition on the tangential velocity [8], is routinely used in science and engineering. Often, the Saffman simplification of the Beavers–Joseph condition neglecting the porous-medium velocity at the interface is considered [23]. An extension of the Beavers–Joseph coupling condition with the symmetrized viscous stress tensor was proposed by Jones [24].

Originally, the Beavers–Joseph coupling condition was proposed for flows

parallel to the fluid–porous interface. Nevertheless, this condition and also its variants are often used for non-parallel flows to the porous layer, e.g., [25, 26]. In [12], it is shown that the Beavers–Joseph condition is not applicable for arbitrary flow directions to the interface that is the case for filtration problems. Besides the unsuitability of the classical coupling conditions for non-parallel flows to the interface, the Beavers–Joseph slip coefficient  $\alpha_{\text{BJ}}$  is uncertain and needs to be determined for every flow problem. Although the question concerning the correct value of the Beavers–Joseph parameter is known for decades, to the best of the authors knowledge, no systematic study on determination of this parameter has been published. In case of cylindrical grains and parallel flows to the porous bed, the optimal value of the Beavers–Joseph slip coefficient was obtained in [27]. In the literature,  $\alpha_{\text{BJ}} = 1$  is typically used even if this is not the optimal choice [12, 28, 29]. However, the correct value of the Beavers–Joseph parameter is essential for accurate numerical simulations of applications, where the Beavers–Joseph condition is applicable, e.g., for microfluidic experiments [30].

Alternative coupling concepts for the Stokes/Darcy problem exist in the literature. However, some of these interface conditions contain unknown model parameters, which still need to be determined before the conditions can be used in numerical simulations, e.g. [4, 19, 22]. Other alternative coupling concepts, where the effective coefficients can be computed based on the pore geometry, are either derived only for unidirectional flows parallel or perpendicular to the porous layer [6, 10, 20] or they are not validated for arbitrary flow directions [7, 31]. An exception is the set of generalized coupling conditions proposed in [21], which is valid for arbitrary flows in coupled free-flow and porous-medium systems. Since the classical interface conditions are still widely used for mathematical modeling and numerical simulation, our goal is to provide an approach for determination of the Beavers–Joseph slip coefficient for those flow problems, when the Beavers–Joseph coupling condition is valid.

In this paper, we deal with the Stokes/Darcy problem using the classical set of interface conditions. We study three different flow problems (pressure-driven flow, lid-driven cavity over porous bed, general filtration problem) with various geometrical configurations of the porous medium (isotropic, orthotropic, anisotropic) and investigate the applicability of the Beavers–Joseph coupling condition comparing macroscale and pore-scale resolved numerical simulation results. For each considered pore geometry, we determine the optimal value of the Beavers–Joseph slip coefficient  $\alpha_{\text{BJ}}$  for unidirectional

flows to the interface. We show that this parameter cannot be fitted for arbitrary flow directions, i.e., the Beavers–Joseph slip coefficient is in general not constant along the fluid–porous interface. Therefore, the Beavers–Joseph condition is unsuitable for arbitrary flows in coupled systems.

The paper is organized as follows. In section 2, we describe the pore-scale resolved and the macroscale coupled flow models and provide the technique to compute the effective permeability. The numerical approach to determine the optimal value of the Beavers–Joseph parameter is presented in section 3. The detailed study of different coupled flow problems is conducted in section 4 and the discussion follows in section 5.

## 2. Mathematical models

In this section, we describe the flow system of interest and present the microscale pore-scale resolved (microscale) and macroscale flow models. The microscale model is used for the determination of the optimal Beavers–Joseph slip coefficient for unidirectional flows and for the validation of the Beavers–Joseph interface condition in section 4. The macroscale model consists of the Stokes/Darcy equations with the classical set of coupling conditions at the sharp fluid–porous interface.

### 2.1. Assumptions on geometry and flow

We consider fluid flow in the coupled domain  $\Omega = \Omega_{\text{ff}} \cup \Omega_{\text{pm}}$  consisting of the free-flow region  $\Omega_{\text{ff}} \subset \mathbb{R}^2$  and the porous medium  $\Omega_{\text{pm}} \subset \mathbb{R}^2$ . The porous layer contains periodically distributed solid inclusions that allows to compute the permeability using the theory of homogenization. We assume the separation of scales, i.e.,  $\varepsilon \ll L$ , where  $\varepsilon$  denotes the characteristic pore size and  $L$  is the length of the domain (fig. 1).

We consider incompressible single-fluid-phase flows at low Reynolds numbers ( $Re \ll 1$ ). The porous medium is supposed to be fully saturated with the same fluid that is present in the free-flow region. From the microscale perspective, the Stokes equations describe the fluid flow in the whole flow domain  $\Omega^\varepsilon = \Omega_{\text{ff}} \cup \Omega_{\text{pm}}^\varepsilon$ , which comprises the free-flow region  $\Omega_{\text{ff}}$  and the pore space  $\Omega_{\text{pm}}^\varepsilon$  of the porous medium (fig. 1, left). At the macroscale, the flow system is divided into two different continuum flow regions separated by the sharp fluid–porous interface  $\Gamma$  (fig. 1, right), which is void of thermodynamic properties. In this case, two different models are applied in the two flow domains and they need to be coupled on the interface  $\Gamma$ .

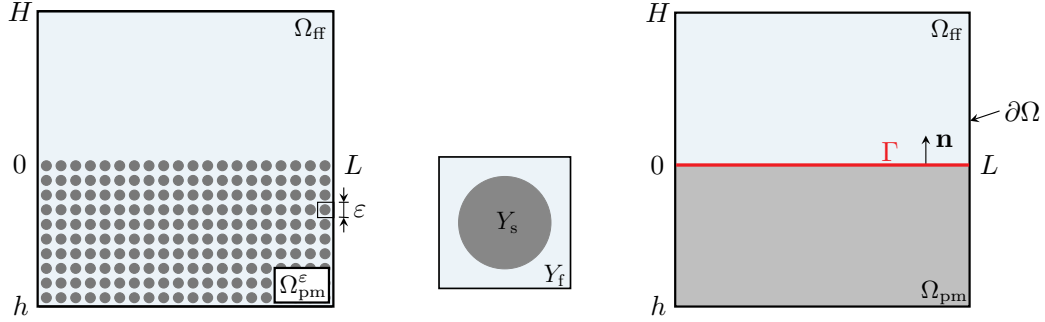


Figure 1: Flow system description at the microscale (left) and macroscale (right). Periodicity cell (middle).

### 2.2. Microscale model

Under the assumptions given in section 2.1, the fluid flow in the whole flow domain  $\Omega^\varepsilon$  is governed by the Stokes equations

$$\nabla \cdot \mathbf{v}^\varepsilon = 0, \quad -\nabla \cdot \mathbf{T}(\mathbf{v}^\varepsilon, p^\varepsilon) - \rho \mathbf{g} = \mathbf{0} \quad \text{in } \Omega^\varepsilon, \quad (1)$$

completed with the no-slip condition on the fluid–solid boundary

$$\mathbf{v}^\varepsilon = \mathbf{0} \quad \text{on } \partial\Omega^\varepsilon \setminus \partial\Omega, \quad (2)$$

and appropriate conditions on the external boundary  $\partial\Omega = \Gamma_D \cup \Gamma_N$ :

$$\mathbf{v}^\varepsilon = \bar{\mathbf{v}} \quad \text{on } \Gamma_D, \quad \mathbf{T}(\mathbf{v}^\varepsilon, p^\varepsilon) \mathbf{n} = \bar{\mathbf{h}} \quad \text{on } \Gamma_N. \quad (3)$$

Here,  $\mathbf{v}^\varepsilon$  and  $p^\varepsilon$  denote the fluid velocity and pressure,  $\rho$  is the fluid density,  $\mathbf{g}$  is the gravitational acceleration,  $\mathbf{T}(\mathbf{v}, p) = 2\mu \mathbf{D}(\mathbf{v}) - p \mathbf{I}$  is the stress tensor,  $\mathbf{D}(\mathbf{v}) = \frac{1}{2} (\nabla \mathbf{v} + (\nabla \mathbf{v})^\top)$  is the rate of strain tensor,  $\mathbf{I}$  is the identity tensor,  $\mu$  is the dynamic viscosity, and  $\bar{\mathbf{v}}$ ,  $\bar{\mathbf{h}}$  are given functions.

### 2.3. Macroscale model

At the macroscale, we consider two different flow domains separated by the sharp interface  $\Gamma$ . Fluid flow in the *free-flow region*  $\Omega_{ff}$  is described by the Stokes equations

$$\nabla \cdot \mathbf{v}_{ff} = 0, \quad -\nabla \cdot \mathbf{T}(\mathbf{v}_{ff}, p_{ff}) - \rho \mathbf{g} = \mathbf{0} \quad \text{in } \Omega_{ff}, \quad (4)$$

where  $\mathbf{v}_{\text{ff}}$  is the fluid velocity and  $p_{\text{ff}}$  is the pressure. On the external boundary of the free-flow region  $\partial\Omega_{\text{ff}} \setminus \Gamma = \Gamma_{D,\text{ff}} \cup \Gamma_{N,\text{ff}}$ , we impose the following boundary conditions

$$\mathbf{v}_{\text{ff}} = \bar{\mathbf{v}} \quad \text{on } \Gamma_{D,\text{ff}}, \quad \mathbf{T}(\mathbf{v}_{\text{ff}}, p_{\text{ff}})\mathbf{n}_{\text{ff}} = \bar{\mathbf{h}} \quad \text{on } \Gamma_{N,\text{ff}}, \quad (5)$$

where  $\mathbf{n}_{\text{ff}}$  is the unit outward normal vector on  $\partial\Omega_{\text{ff}}$ .

Fluid flow through the *porous medium* is described by the Darcy flow equations

$$\nabla \cdot \mathbf{v}_{\text{pm}} = 0, \quad \mathbf{v}_{\text{pm}} = -\frac{\mathbf{K}}{\mu} (\nabla p_{\text{pm}} - \rho \mathbf{g}) \quad \text{in } \Omega_{\text{pm}}, \quad (6)$$

where  $\mathbf{v}_{\text{pm}}$  is the Darcy velocity,  $p_{\text{pm}}$  is the fluid pressure and  $\mathbf{K}$  is the intrinsic permeability tensor, which is symmetric, positive definite and bounded. The following boundary conditions are prescribed on the external boundary of the porous-medium domain  $\partial\Omega_{\text{pm}} \setminus \Gamma = \Gamma_{D,\text{pm}} \cup \Gamma_{N,\text{pm}}$ :

$$p_{\text{pm}} = \bar{p} \quad \text{on } \Gamma_{D,\text{pm}}, \quad \mathbf{v}_{\text{pm}} \cdot \mathbf{n}_{\text{pm}} = \bar{v} \quad \text{on } \Gamma_{N,\text{pm}}, \quad (7)$$

where  $\Gamma_{D,\text{pm}} \cap \Gamma_{N,\text{pm}} = \emptyset$ ,  $\mathbf{n}_{\text{pm}}$  is the unit outward normal vector on  $\partial\Omega_{\text{pm}}$  and  $\bar{p}$ ,  $\bar{v}$  are given functions. Within this work, we neglect the gravitational effects setting  $\mathbf{g} = \mathbf{0}$  in equations (1), (4) and (6).

In addition to the boundary conditions on the external boundary of the coupled domain  $\partial\Omega$ , appropriate *interface conditions* have to be set on the fluid–porous interface  $\Gamma$ . In this paper, we consider the classical set of coupling conditions consisting of the conservation of mass across the interface (8), the balance of normal forces (9) and the Beavers–Joseph condition (10) for the tangential velocity component

$$\mathbf{v}_{\text{ff}} \cdot \mathbf{n} = \mathbf{v}_{\text{pm}} \cdot \mathbf{n} \quad \text{on } \Gamma, \quad (8)$$

$$-\mathbf{n} \cdot \mathbf{T}(\mathbf{v}_{\text{ff}}, p_{\text{ff}}) \mathbf{n} = p_{\text{pm}} \quad \text{on } \Gamma, \quad (9)$$

$$(\mathbf{v}_{\text{ff}} - \mathbf{v}_{\text{pm}}) \cdot \boldsymbol{\tau} - \frac{\sqrt{\mathbf{K}}}{\alpha_{\text{BJ}}} \mathbf{D}(\mathbf{v}_{\text{ff}}) \mathbf{n} \cdot \boldsymbol{\tau} = 0 \quad \text{on } \Gamma. \quad (10)$$

Here,  $\mathbf{n} = -\mathbf{n}_{\text{ff}} = \mathbf{n}_{\text{pm}}$  is the unit vector normal to the fluid–porous interface  $\Gamma$  pointing outward from the porous-medium domain  $\Omega_{\text{pm}}$  (fig. 1, right),  $\boldsymbol{\tau}$  is a unit vector tangential to the interface and  $\alpha_{\text{BJ}} > 0$  is the Beavers–Joseph slip coefficient.

#### 2.4. Effective model parameters

In order to obtain computable macroscale models, which reflect the corresponding flow processes at the microscale, effective parameters need to be determined. In our case, these are the exact position of the fluid–porous interface  $\Gamma$ , the permeability tensor  $\mathbf{K}$  and the Beavers–Joseph slip coefficient  $\alpha_{\text{BJ}}$ .

Within this paper, we consider the fluid–porous interface positioned tangential to the top of the first row of solid inclusions as suggested in [8]. This location of the sharp interface was also recommended in [7, 29].

In order to compute the permeability tensor  $\mathbf{K} = (k_{ij})_{i,j=1,2}$ , we apply the theory of homogenization [32]. This leads to

$$k_{ij} = \varepsilon^2 \tilde{k}_{ij}, \quad \tilde{k}_{ij} = \int_{Y_{\text{f}}} w_i^j(\mathbf{y}) \, d\mathbf{y}, \quad (11)$$

where  $Y_{\text{f}}$  is the fluid part of the periodicity cell  $Y = (0, 1) \times (0, 1) = Y_{\text{f}} \cup Y_{\text{s}}$  (fig. 1, middle) and  $\mathbf{w}^j = (w_1^j, w_2^j)$  are the solutions to the cell problems

$$\begin{aligned} \nabla_{\mathbf{y}} \cdot \mathbf{w}^j &= 0, \quad -\Delta_{\mathbf{y}} \mathbf{w}^j + \nabla_{\mathbf{y}} \pi^j = \mathbf{e}_j \quad \text{in } Y_{\text{f}}, \quad \int_{Y_{\text{f}}} \pi^j \, d\mathbf{y} = 0, \\ \mathbf{w}^j &= \mathbf{0} \quad \text{on } \partial Y_{\text{f}} \setminus \partial Y, \quad \{\mathbf{w}^j, \pi^j\} \text{ is 1-periodic in } \mathbf{y}, \quad \mathbf{y} = \mathbf{x}/\varepsilon, \end{aligned} \quad (12)$$

for  $j = 1, 2$ .

To determine the optimal Beavers–Joseph slip coefficient  $\alpha_{\text{BJ}}$ , we minimize the error between the macroscale and the pore-scale resolved numerical simulation results using the Clough–Tocher interpolation and simulated annealing. The numerical optimization strategy is described in section 3.

### 3. Computation of the Beavers–Joseph slip coefficient

To compute the Beavers–Joseph slip coefficient  $\alpha_{\text{BJ}}$ , we compare the pore-scale resolved numerical simulations to the macroscale simulations. The optimal Beavers–Joseph parameter is found when the macroscale simulation results provide the smallest relative error to the microscale results. In this section, we present the mathematical methods for determination of the optimal value of the slip coefficient  $\alpha_{\text{BJ}}$ .

### 3.1. Clough–Tocher interpolation

The microscale and the macroscale velocities and pressures are computed on different meshes. Due to the presence of solid obstacles at the microscale, an adaptive triangular mesh is applied in the whole fluid domain  $\Omega^\varepsilon$  for the pore-scale resolved simulations. The macroscale solutions are computed on the staggered Cartesian mesh in the coupled domain  $\Omega$ .

To compare the microscale and macroscale solutions, we interpolate the pore-scale simulation results using the Clough–Tocher interpolation which provides  $C^1$ -functions and operates on triangulated data. On each triangle with vertices  $\mathbf{V}_1$ ,  $\mathbf{V}_2$  and  $\mathbf{V}_3$  (fig. 2, left) a cubic polynomial is constructed. The centroid of the triangle is given by  $\mathbf{V}_4 = (\mathbf{V}_1 + \mathbf{V}_2 + \mathbf{V}_3)/3$ . Every point inside the triangle can be expressed by an extension of the barycentric coordinates

$$\mathbf{P} = \sum_{i=1}^4 b_i \mathbf{V}_i, \quad (13)$$

where

$$\sum_{i=1}^4 b_i = 1, \quad \prod_{i=1}^3 b_i = 0, \quad b_i \geq 0, \quad i = 1, \dots, 4. \quad (14)$$

The piecewise cubic Bezier interpolant  $f_{\text{int}}$  can be written as

$$f_{\text{int}}(\mathbf{P}) = \sum_{i+j+k+l=3} \frac{3!}{i! j! k! l!} c_{ijkl} b_1^i b_2^j b_3^k b_4^l, \quad (15)$$

where the Clough–Tocher scheme [33] is applied to compute the coefficients  $c_{ijkl}$  associated with the points  $\mathbf{C}_{ijkl} = (i\mathbf{V}_1 + j\mathbf{V}_2 + k\mathbf{V}_3 + l\mathbf{V}_4)/3$  (fig. 2, right). Continuity between the triangles is ensured by the interpolation. To obtain differentiability at the sides of the triangles we require the first order normal derivative on each edge to be linear. The normal on the edge  $\mathbf{e}_{ij}$  is given by  $\mathbf{n}_k = \mathbf{e}_{i4} + \beta_k \mathbf{e}_{ij}$ , where  $\beta_k$  is taken so that the condition  $\mathbf{n}_k \cdot \mathbf{e}_{ij} = 0$  is satisfied, i.e.,  $\beta_k = -(\mathbf{e}_{i4} \cdot \mathbf{e}_{ij}) / \|\mathbf{e}_{ij}\|^2$ .



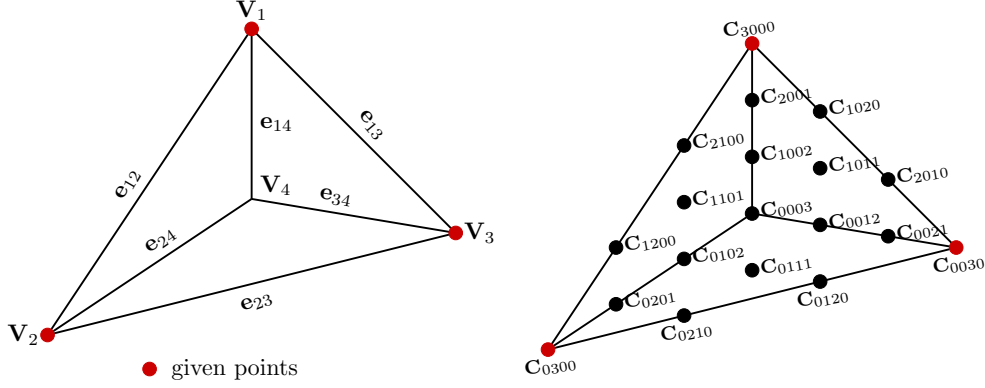


Figure 2: Triangulation and positions of points  $C_{ijkl}$ .

We define the normal derivative according to [34]:

$$\begin{aligned}
& \frac{\partial f}{\partial \mathbf{n}_k} ((1-t)\mathbf{V}_i + t\mathbf{V}_j) \\
&= (1-t) \left( \frac{(x_{2,j} - x_{2,i}) \frac{\partial f}{\partial x_1}(\mathbf{V}_i) - (x_{1,j} - x_{1,i}) \frac{\partial f}{\partial x_2}(\mathbf{V}_i)}{\|\mathbf{e}_{ij}\|} \right) \\
&+ t \left( \frac{(x_{2,j} - x_{2,i}) \frac{\partial f}{\partial x_1}(\mathbf{V}_j) - (x_{1,j} - x_{1,i}) \frac{\partial f}{\partial x_2}(\mathbf{V}_j)}{\|\mathbf{e}_{ij}\|} \right), \tag{16}
\end{aligned}$$

where  $\mathbf{V}_i = (x_{1,i}, x_{2,i})$ ,  $\mathbf{V}_j = (x_{1,j}, x_{2,j})$ ,  $\|\mathbf{e}_{ij}\|$  is the length of the edge  $\mathbf{e}_{ij} = \mathbf{V}_j - \mathbf{V}_i$ , and  $t \in (0, 1)$ .

The Clough–Tocher interpolation scheme has the property of being local. That means the value of the interpolant at a given point only depends on data points close to the given point. Therefore, even a huge amount of data can be interpolated fast.

### 3.2. Simulated annealing

To determine the optimal Beavers–Joseph slip coefficient  $\alpha_{\text{BJ}}$  we minimize the relative error between the macroscale and the pore-scale resolved solutions. The errors are defined along the fixed cross section  $x_1 = c$  as follows

$$\epsilon_{f,c} = \frac{\|f(c, \cdot) - f^\varepsilon(c, \cdot)\|}{\|f^\varepsilon(c, \cdot)\|}, \quad \|f(c, \cdot)\|^2 = \int_h^H f(c, x_2)^2 dx_2, \tag{17}$$

where  $f^\varepsilon$  is the solution of the pore-scale resolved problem and  $f$  is the solution of the macroscale problem.

We use simulated annealing (Algorithm 1) to minimize the relative error  $\epsilon_{f,c}$  given in (17). To accelerate the minimization process, we propose the following two-stage procedure. First, Algorithm 1 is applied for the range  $\alpha_{\text{BJ}} \in \{0.01, 1, 2, \dots, M\}$  in order to find the interval  $[\alpha_i, \alpha_{i+1}]$ , which contains the optimal value  $\alpha_{\text{BJ}}^{\text{opt}}$ . We take  $\alpha_0 = 0.01$  due to  $\alpha_{\text{BJ}} > 0$  and  $\alpha_i = i$  for  $i = 1, \dots, M$  with  $M \in \mathbb{N}$ . If the optimal value  $\alpha_{\text{BJ}}^{\text{opt}} \in \mathbb{N}$ , we are done, otherwise, we make a second step. We consider the following candidates for the optimal Beavers–Joseph parameter:  $\alpha_{i+1} - 0.1j$ ,  $j = 1, \dots, 9$  and take the one yielding the smallest error (17). Since the error is changing only slightly when considering more candidates in the interval  $[\alpha_i, \alpha_{i+1}]$  for the numerical simulation results presented in section 4, it is sufficient to determine  $\alpha_{\text{BJ}}^{\text{opt}}$  up to the first digit after comma in our case.

---

**Algorithm 1** (Simulated annealing)

---

Choose  $x_0 \in \mathbb{R}$  and set  $A_0 = 1$ ,  $c_{\text{grow}} > 1$ ,  $c_{\text{shrink}} < 1$   
Choose a monotonically decreasing null sequence  $(T_k)_{k \in \mathbb{N}_0}$   
 $x_{\text{approx}} = x_0$ ,  $x_{\text{opt}} = x_0$ ,  $k = 0$   
**repeat**  
  Choose  $r_k \sim \mathcal{N}(0, 1)$ ,  $x_{k+1} = x_k + A_k r_k$   
  **if**  $\epsilon_{f,c}(x_{k+1}) \leq \epsilon_{f,c}(x_{\text{approx}})$  **then**  
     $x_{\text{approx}} = x_{k+1}$ ,  $A_{k+1} = A_k c_{\text{grow}}$   
  **else if**  $\text{rand}([0, 1]) < e^{(\epsilon_{f,c}(x_{k+1}) - \epsilon_{f,c}(x_{\text{opt}}))/T_k}$  **then**  
     $x_{\text{approx}} = x_{k+1}$ ,  $A_{k+1} = A_k c_{\text{grow}}$   
  **else**  
     $A_{k+1} = A_k c_{\text{shrink}}$   
  **end if**  
  **if**  $\epsilon_{f,c}(x_{\text{approx}}) < \epsilon_{f,c}(x_{\text{opt}})$  **then**  
     $x_{\text{opt}} = x_{\text{approx}}$   
  **end if**  
   $k = k + 1$   
**until**  $T_k < \varepsilon_{\text{tol}}$  OR  $k < k_{\text{max}}$

---

In Algorithm 1, we choose the monotonically decreasing null sequence  $T_k = ae^{-k/b}$  with  $a = 0.005$  and  $b = 100$ . We set  $c_{\text{grow}} = 1.1$ ,  $c_{\text{shrink}} = 0.99$ ,  $\varepsilon_{\text{tol}} = 10^{-12}$  and  $k_{\text{max}} = 10^5$ .

## 4. Numerical results

In this section, we study the dependency of the Beavers–Joseph slip coefficient  $\alpha_{\text{BJ}}$  on the flow scenario and the pore-scale geometrical information, and determine the optimal value of  $\alpha_{\text{BJ}}$  for unidirectional flows. We consider three different flow problems: i) fluid flow is parallel to the porous layer (pressure-driven flow); ii) flow is mainly parallel to the porous medium (lid-driven cavity over porous bed); and iii) flow is arbitrary to the fluid–porous interface (general filtration).

We study various porous-medium geometrical configurations considering different shapes of solid inclusions (circular, elliptical, rectangular) and different arrangements of solid grains (in-line, staggered) leading to isotropic, orthotropic and anisotropic media. To analyze the dependency of the Beavers–Joseph parameter on porosity, permeability and pore-scale surface roughness we consider different pore geometries, which lead to the same porosity and permeability (table 1, geometries  $G_1$  and  $G_3$ ); porous media containing the same type of solid inclusions of different sizes which result in different permeability and porosity (table 1, geometries  $G_1$ ,  $G_2$  and  $G_4$ ); and pore geometries having the same porosity but different permeability tensors (table 1, geometries  $G_1$ ,  $G_4$  and  $G_5$ ,  $G_6$ ). All considered porous-medium geometries are periodic such that homogenization theory can be applied to compute the permeability tensor using formula (11). We set the dynamic viscosity of the fluid  $\mu = 1$  for all flow problems.

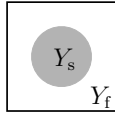
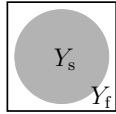
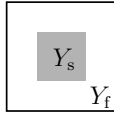
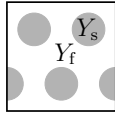
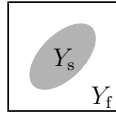
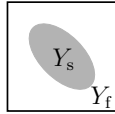
	$G_1$	$G_2$	$G_3$	$G_4$	$G_5$	$G_6$
						
$\tilde{k}_{11}$	$1.99 \cdot 10^{-2}$	$5.67 \cdot 10^{-4}$	$1.99 \cdot 10^{-2}$	$5.63 \cdot 10^{-3}$	$1.23 \cdot 10^{-2}$	$1.23 \cdot 10^{-2}$
$\tilde{k}_{12}$	0	0	0	0	$2.69 \cdot 10^{-3}$	$-2.69 \cdot 10^{-3}$
$\tilde{k}_{22}$	$1.99 \cdot 10^{-2}$	$5.67 \cdot 10^{-4}$	$1.99 \cdot 10^{-2}$	$4.44 \cdot 10^{-3}$	$1.23 \cdot 10^{-2}$	$1.23 \cdot 10^{-2}$
$\phi$	0.80	0.40	0.81	0.80	0.75	0.75

Table 1: Scaled permeability values  $\tilde{k}_{ij}$  and porosity  $\phi$  for different porous-medium configurations.

The microscale problem (1)–(3) and the unit cell Stokes problems (12)

are solved using the software package FREEFEM++ with the Taylor–Hood finite elements [35]. The macroscale problem (4)–(10) is discretized using the finite volume method on staggered Cartesian grids conforming at the fluid–porous interface with the grid size  $h = 1/800$ .

In the following, we show that for unidirectional flows parallel to the fluid–porous interface an optimal Beavers–Joseph parameter can be found, whereas for arbitrary flow directions the slip coefficient  $\alpha_{\text{BJ}}$  cannot be fitted along the interface.

#### 4.1. Pressure-driven flow

In this section, we study a flow scenario where the flow is parallel to the fluid–porous interface (pressure-driven flow). We consider the free-flow domain  $\Omega_{\text{ff}} = [0, 1] \times [0, 0.5]$ , the porous medium  $\Omega_{\text{pm}} = [0, 1] \times [-0.5, 0]$  and the sharp fluid–porous interface  $\Gamma = [0, 1] \times \{0\}$ . We analyze different porous-medium geometries (table 1), different orders of velocity magnitude and different characteristic pore sizes  $\varepsilon$  in order to study the influence of the pore-scale interface roughness, permeability  $\mathbf{K}$ , porosity  $\phi$  and the free-flow regime on the Beavers–Joseph slip coefficient  $\alpha_{\text{BJ}}$ .

To compute the permeability for geometry  $G_1$ , the unit cell problems (12) are solved using an adaptive mesh, where the fluid part  $Y_f$  is partitioned into approximately 35 000 elements. For solving the pore-scale problem (1)–(3) in the whole flow domain, an adaptive mesh with approximately 330 000 elements is used. We set the upper boundary  $M = 10$  for the Beavers–Joseph slip coefficient in the minimization procedure described in section 3.2 in order to consider a broader range of values in comparison to [8].

To describe a pressure-driven flow, we impose the following boundary conditions for the microscale model (1)–(3):

$$\bar{\mathbf{v}} = \mathbf{0} \quad \text{on} \quad \Gamma_D, \quad \bar{\mathbf{h}} = (0, -31.75) \quad \text{on} \quad \Gamma_N^{\text{in}}, \quad \bar{\mathbf{h}} = \mathbf{0} \quad \text{on} \quad \Gamma_N^{\text{out}}, \quad (18)$$

where  $\Gamma_N^{\text{in}} = \{0\} \times (-0.5, 0.5)$ ,  $\Gamma_N^{\text{out}} = \{1\} \times (-0.5, 0.5)$ ,  $\Gamma_D = \partial\Omega \setminus (\Gamma_N^{\text{in}} \cup \Gamma_N^{\text{out}})$ . For the coupled macroscale model (4)–(10), we set

$$\begin{aligned} \bar{\mathbf{v}} = \mathbf{0} & \quad \text{on} \quad \Gamma_{D,\text{ff}}, & \bar{v} = 0 & \quad \text{on} \quad \Gamma_{N,\text{pm}}, \\ \bar{\mathbf{h}} = (0, -31.75) & \quad \text{on} \quad \Gamma_{N,\text{ff}}^{\text{in}}, & \bar{p} = 31.75 & \quad \text{on} \quad \Gamma_{D,\text{pm}}^{\text{in}}, \\ \bar{\mathbf{h}} = \mathbf{0} & \quad \text{on} \quad \Gamma_{N,\text{ff}}^{\text{out}}, & \bar{p} = 0 & \quad \text{on} \quad \Gamma_{D,\text{pm}}^{\text{out}}, \end{aligned} \quad (19)$$

where  $\Gamma_{D,\text{ff}} = \Gamma_D \cap \partial\Omega_{\text{ff}}$ ,  $\Gamma_{N,\text{pm}} = \Gamma_D \cap \partial\Omega_{\text{pm}}$ ,  $\Gamma_{N,\text{ff}}^{\text{in/out}} = \Gamma_N^{\text{in/out}} \cap \partial\Omega_{\text{ff}}$ , and  $\Gamma_{D,\text{pm}}^{\text{in/out}} = \Gamma_N^{\text{in/out}} \cap \partial\Omega_{\text{pm}}$ .

Boundary conditions (18) and (19) lead to unidirectional flows parallel to the fluid–porous interface, where the normal component of velocity is zero and the pressure field is linear. For this flow problem, the macroscale pressure and the normal velocity component do not depend on the choice of the Beavers–Joseph parameter. Therefore, we provide velocity profiles only for the tangential velocity component in the middle of the coupled domain at  $x_1 = 0.5$ .

#### 4.1.1. Geometry $G_1$ , $\varepsilon = 1/20$

In this case, the porous medium is constructed by  $20 \times 10$  periodically distributed circular solid inclusions presented in table 1, which are arranged in line (fig. 3, left). This yields the characteristic pore size  $\varepsilon = 1/20$  and the radius of inclusions is  $r = 0.25\varepsilon$ . The described pore-scale geometrical configuration leads to a highly porous ( $\phi = 0.8$ ) isotropic medium with the permeability tensor  $\mathbf{K} = \text{diag}\{k_{11}, k_{11}\}$ , where  $\mathbf{K} = \varepsilon^2 \tilde{\mathbf{K}}$  (table 1).

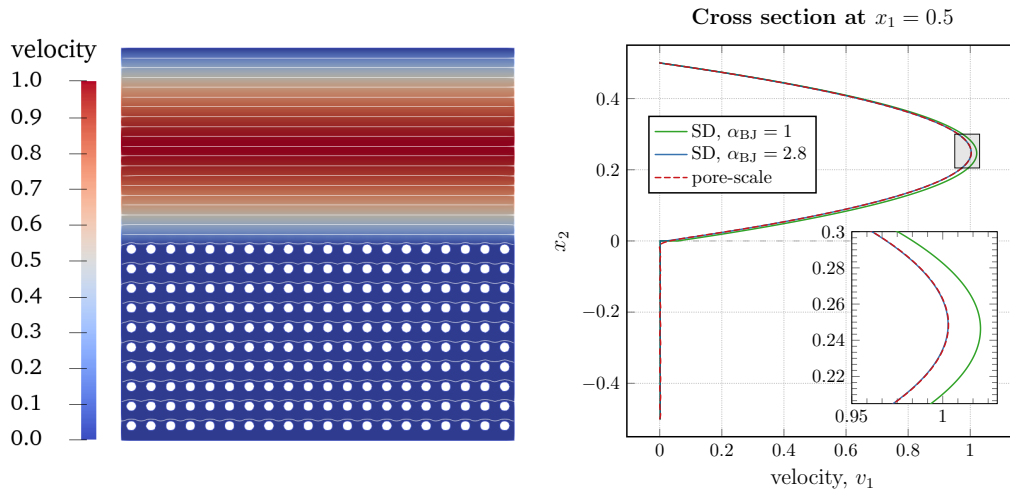


Figure 3: Microscale velocity field (left) and tangential velocity profiles (right) for the pressure-driven flow and geometry  $G_1$ .

The pore-scale velocity field is presented in fig. 3 (left). The optimal value of the Beavers–Joseph slip coefficient is  $\alpha_{\text{BJ}}^{\text{opt}} = 2.8$ . In fig. 3 (right), we compare two macroscale Stokes/Darcy problems (4)–(10) with the standard value of the Beavers–Joseph parameter  $\alpha_{\text{BJ}} = 1$  (profile: SD,  $\alpha_{\text{BJ}} = 1$ ) and the optimal value  $\alpha_{\text{BJ}}^{\text{opt}} = 2.8$  (profile: SD,  $\alpha_{\text{BJ}} = 2.8$ ) against the pore-scale

resolved simulations (profile: pore-scale). The relative errors between the pore-scale and the macroscale simulation results for these two values of  $\alpha_{\text{BJ}}$  are presented in table 2.

The optimal value of the Beavers–Joseph slip coefficient  $\alpha_{\text{BJ}}$  is independent of velocity magnitude. Several variants of  $\bar{\mathbf{h}}$  and  $\bar{p}$  in the boundary conditions (18) and (19) have been analyzed, all leading to the same optimal parameter  $\alpha_{\text{BJ}}^{\text{opt}} = 2.8$ .

#### 4.1.2. Geometry $G_2$ , $\varepsilon = 1/20$

In order to obtain a moderate porosity  $\phi = 0.4$ , we increase the radius of solid inclusions in comparison to the previous example. In this case, we consider  $20 \times 10$  circular solid inclusions with radius  $r = \varepsilon\sqrt{(1 - \phi)}/\pi$  arranged in line (fig. 4, left). This geometrical configuration leads again to an isotropic porous medium and the permeability values are presented in table 1. For this pore geometry, we obtained the optimal value of the Beavers–Joseph parameter  $\alpha_{\text{BJ}}^{\text{opt}} = 0.5$  (table 2).

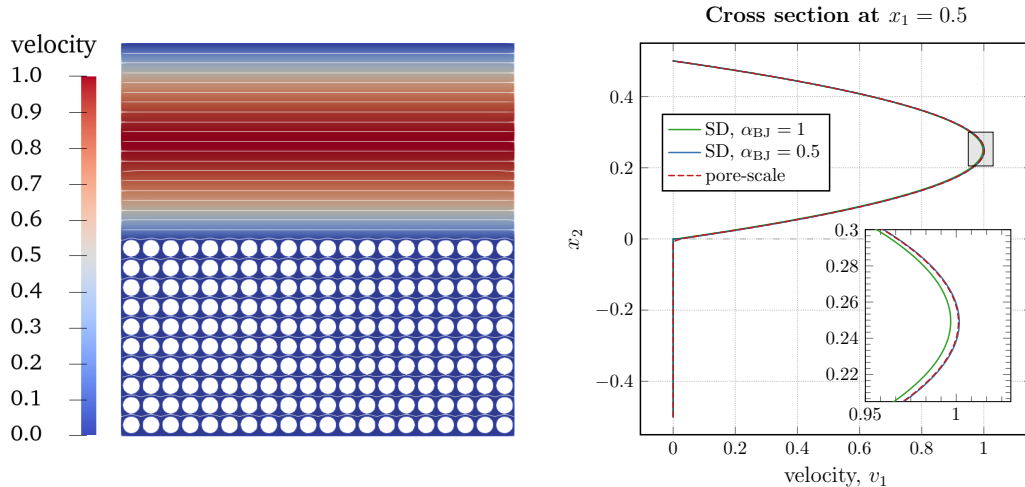


Figure 4: Microscale velocity field (left) and tangential velocity profiles (right) for the pressure-driven flow and geometry  $G_2$ .

#### 4.1.3. Geometry $G_3$ , $\varepsilon = 1/20$

We study the dependence of the Beavers–Joseph parameter on the effective properties (porosity, permeability) and the porous-medium morphology

leading to different pore-scale interface roughness. Therefore, we construct a porous medium which has the same permeability and porosity as geometry  $G_1$  but different shape of solid inclusions. We consider a porous medium consisting of  $20 \times 10$  in-line arranged squared solid inclusions with length  $a = 0.2154 \varepsilon$  leading to an isotropic medium (table 1).

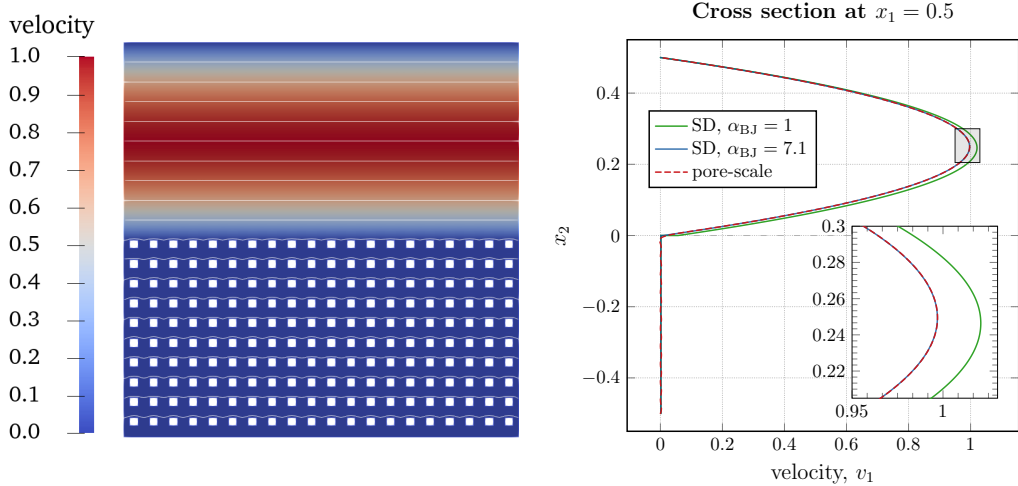


Figure 5: Microscale velocity field (left) and tangential velocity profiles (right) for the pressure-driven flow and geometry  $G_3$ .

We provide the pore-scale velocity field and the profiles of the tangential velocity component in the middle of the domain in fig. 5. The optimal value of the Beavers–Joseph parameter for this configuration is found to be  $\alpha_{\text{BJ}}^{\text{opt}} = 7.1$  (table 2). Comparing this result with the one for geometry  $G_1$  ( $\alpha_{\text{BJ}}^{\text{opt}} = 2.8$ ) having the same permeability and porosity but different pore morphology, we conclude that  $\alpha_{\text{BJ}}$  depends not only on the effective properties of the medium but also on the pore geometry and microscale surface roughness.

#### 4.1.4. Geometry $G_4$ , $\varepsilon = 1/10$

In this test case, we construct a porous medium having the same surface roughness as geometry  $G_1$  with  $\varepsilon = 1/20$  but different permeability. For this purpose, we consider  $20 \times 10$  circular solid inclusions arranged in a staggered manner (table 1, fig. 6). This leads to  $\varepsilon = 1/10$  and to an orthotropic porous medium with  $\mathbf{K} = \text{diag}\{k_{11}, k_{22}\}$ ,  $k_{11} \neq k_{22}$ . The radius of the circular solid grains is  $r = 0.125 \varepsilon$  and the permeability values are given in table 1.

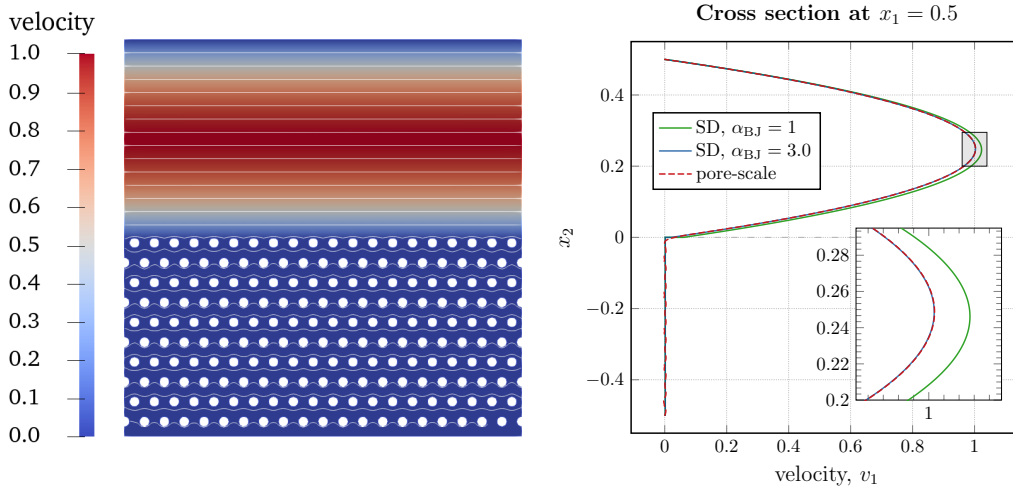


Figure 6: Microscale velocity field (left) and tangential velocity profiles (right) for the pressure-driven flow and geometry  $G_4$ .

For orthotropic porous media, there exist different approaches in the literature, e.g., [5, 12, 36] to compute  $\sqrt{\mathbf{K}}$  appearing in the interface condition (10). The first one is to take  $\sqrt{\mathbf{K}} = \sqrt{\boldsymbol{\tau} \cdot \mathbf{K} \boldsymbol{\tau}}$ , which leads to  $\sqrt{\mathbf{K}} = \sqrt{k_{11}}$  for our setting. The second interpretation is  $\sqrt{\mathbf{K}} = \sqrt{\text{tr}(\mathbf{K})/d}$ , where  $d$  is the number of space dimensions. In our case, we obtain  $\sqrt{\mathbf{K}} = \sqrt{(k_{11} + k_{22})/2}$ . The optimal values of  $\alpha_{\text{BJ}}$  for these two cases are presented in table 2. The choice of  $\sqrt{\mathbf{K}}$  influences the optimal Beavers–Joseph parameter, however the ratio  $\sqrt{\mathbf{K}}/\alpha_{\text{BJ}}$  is the same. Therefore, in fig. 6 (right), we present only the macroscale simulation results for the first approach  $\sqrt{\mathbf{K}} = \sqrt{k_{11}}$ .

Note that taking the second approach to compute  $\sqrt{\mathbf{K}}$  we obtain the same value  $\alpha_{\text{BJ}}^{\text{opt}} = 2.8$  as in section 4.1.1, where the microscale surface roughness is exactly the same.

#### 4.1.5. Geometries $G_5$ and $G_6$ , $\varepsilon = 1/20$

We consider two anisotropic porous media with full permeability tensors  $\mathbf{K}$ . The porous media are composed by  $20 \times 10$  elliptical solid inclusions arranged in line ( $\varepsilon = 1/20$ ) tilted to the right (table 1, geometry  $G_5$ ) and tilted to the left (table 1, geometry  $G_6$ ). The semi-axes are  $a = 0.4\varepsilon$  and  $b = 0.2\varepsilon$  and the ellipses are rotated clockwise and counter-clockwise by  $45^\circ$ , respectively. Geometries  $G_5$  and  $G_6$  lead to different permeability tensors (table 1), however, the value of  $\sqrt{\mathbf{K}} = \sqrt{\boldsymbol{\tau} \cdot \mathbf{K} \boldsymbol{\tau}}$  in the Beavers–Joseph con-



dition (10) is the same for our setting. Both geometries provide the same interface roughness.

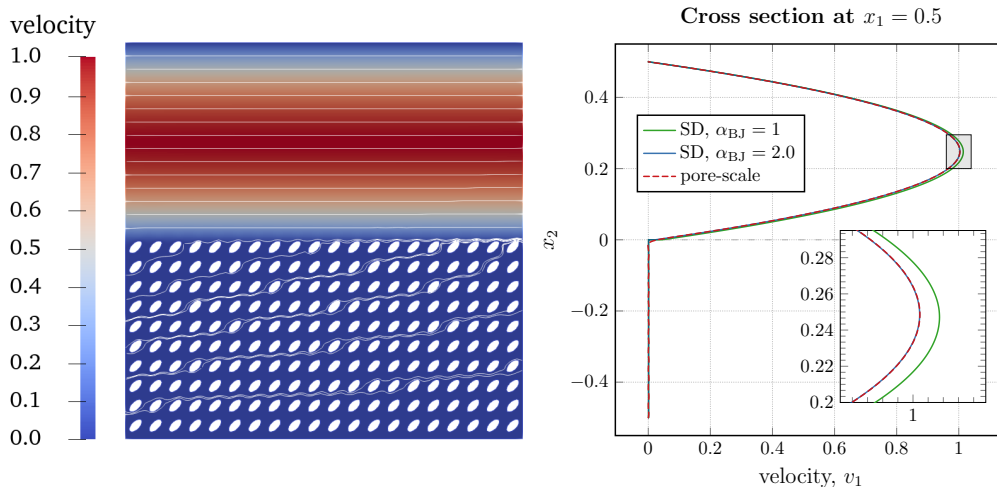


Figure 7: Microscale velocity field (left) and tangential velocity profiles (right) for the pressure-driven flow and geometry  $G_5$ .

We obtain the same optimal value of the Beavers–Joseph slip coefficient  $\alpha_{\text{BJ}}^{\text{opt}} = 2.0$  (table 2) for both geometries. Therefore, we only present the macroscale simulation results for geometry  $G_5$  in fig. 7 (right).

#### 4.1.6. Geometry $G_1$ with different values for $\varepsilon$

In this test case, we study the impact of the characteristic pore size  $\varepsilon$  and consequently the permeability  $\mathbf{K}$  on the Beavers–Joseph parameter  $\alpha_{\text{BJ}}$ . We consider circular solid inclusions  $G_1$  and construct two porous media in addition to the one considered in section 4.1.1: the porous layer having  $40 \times 20$  in-line arranged circular solid inclusions ( $\varepsilon = 1/40$ ) and  $80 \times 40$  inclusions ( $\varepsilon = 1/80$ ). In both cases, the radius of the solid grains is  $r = 0.25\varepsilon$ . Compared to section 4.1.1 with  $\varepsilon = 1/20$ , we have the same porosity but smaller characteristic pore sizes leading to smaller permeability of the porous media. The pore-scale surface roughness for these media is also different.

For the porous-medium geometrical configuration with characteristic pore size  $\varepsilon = 1/40$  the optimal Beavers–Joseph slip coefficient is  $\alpha_{\text{BJ}}^{\text{opt}} = 2.7$  and in case of  $\varepsilon = 1/80$  the optimal value is  $\alpha_{\text{BJ}}^{\text{opt}} = 2.6$  (table 2). Considering also the results obtained for geometry  $G_1$  with  $\varepsilon = 1/20$ , we can conclude that in case of the same type of solid inclusions and the same porosity but

different permeability the optimal value of the Beavers–Joseph parameter changes only slightly.

The pore-scale velocity field and the profiles of the tangential velocity component in the middle of the domain are presented in fig. 8 for both geometrical configurations. From these plots and the ones in fig. 3 we observe that the macroscale profile with  $\alpha_{\text{BJ}} = 1$  provides a better fit to the pore-scale simulation results for smaller  $\varepsilon$ . This observation is in accordance to

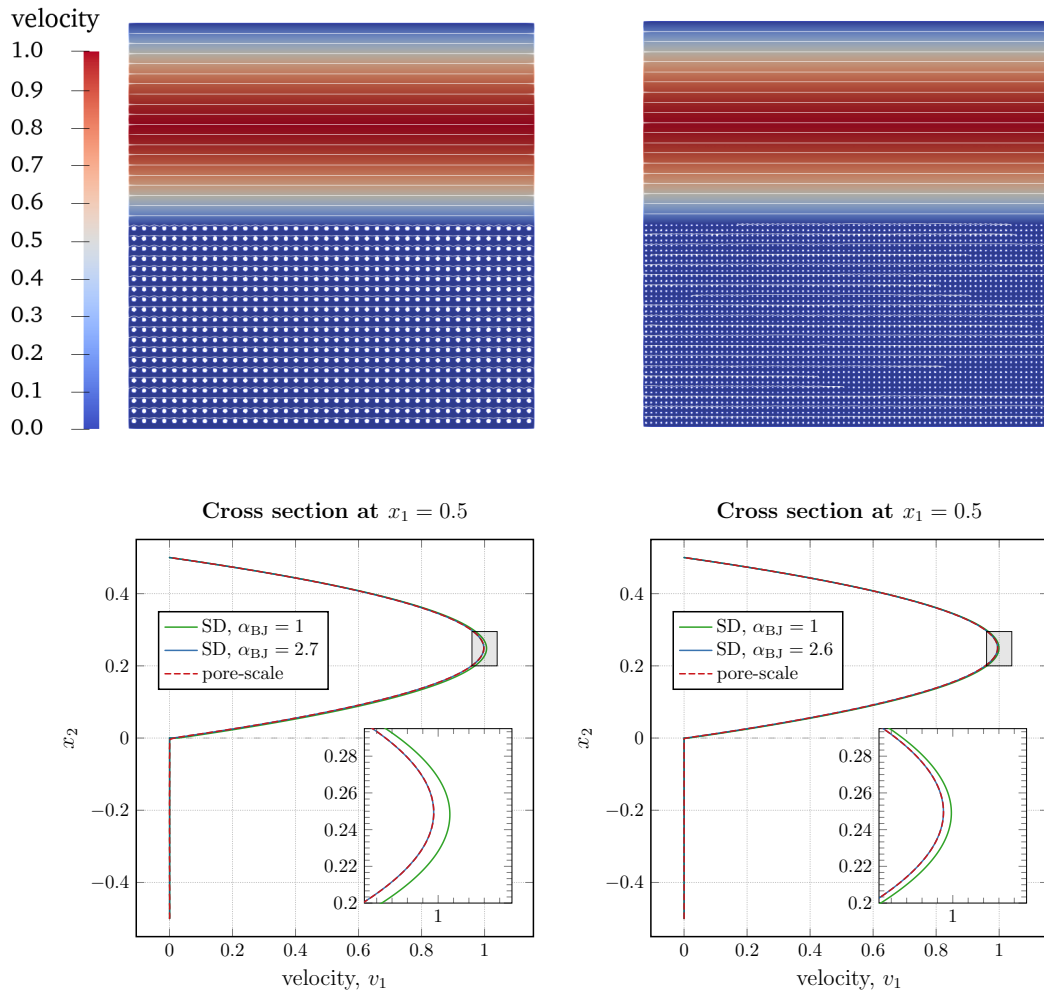


Figure 8: Microscale velocity fields and tangential velocity profiles for the pressure-driven flow and geometry  $G_1$  for  $\varepsilon = 1/40$  (left) and  $\varepsilon = 1/80$  (right).

the physics since for  $\varepsilon \rightarrow 0$  we are approaching the no-slip condition on the solid wall. In this case, the value of the Beavers–Joseph parameter becomes less relevant.

In table 2, we summarize the optimal Beavers–Joseph parameters  $\alpha_{\text{BJ}}^{\text{opt}}$  and the relative errors  $\epsilon_{v_1,0.5}$  for the tangential velocity for the pressure-driven flow and different pore geometries.

<b>Geometry</b>	$\alpha_{\text{BJ}}^{\text{opt}}$	<b>Error for <math>\alpha_{\text{BJ}}^{\text{opt}}</math></b>	<b>Error for <math>\alpha_{\text{BJ}} = 1</math></b>
$G_1, \varepsilon = 1/20$	2.8	0.003401	0.027937
$G_1, \varepsilon = 1/40$	2.7	0.001201	0.013857
$G_1, \varepsilon = 1/80$	2.6	0.000405	0.006781
$G_2$	0.5	0.002838	0.006941
$G_3$	7.1	0.002632	0.037578
$G_4, \sqrt{\mathbf{K}} = \sqrt{k_{11}}$	3.0	0.004092	0.030885
$G_4, \sqrt{\mathbf{K}} = \sqrt{(k_{11} + k_{22})/2}$	2.8	0.004098	0.028440
$G_5$	2.0	0.002901	0.017375
$G_6$	2.0	0.002901	0.017375

Table 2: Optimal Beavers–Joseph parameters  $\alpha_{\text{BJ}}^{\text{opt}}$  and relative errors between the pore-scale and macroscale simulation results  $\epsilon_{v_1,0.5}$  given in (17) for the pressure-driven flow and different porous-medium geometries.

#### 4.2. Lid-driven cavity over porous bed

In this section, we investigate the lid-driven cavity over porous bed. The free-flow region  $\Omega_{\text{ff}} = [0, 1] \times [0, 1]$  is separated from the porous-medium domain  $\Omega_{\text{pm}} = [0, 1] \times [-0.5, 0]$  by the fluid–porous interface  $\Gamma = [0, 1] \times \{0\}$ . We consider the porous-medium geometry  $G_2$  with the characteristic pore size  $\varepsilon = 1/40$  inspired by the setting in [29].

For this test case, we consider the following boundary conditions on the external boundary  $\partial\Omega$  for the microscale model (1)–(3):

$$\bar{\mathbf{v}} = (1, 0) \text{ on } \Gamma_D^{\text{in}}, \quad \bar{\mathbf{v}} = \mathbf{0} \text{ on } \Gamma_D^{\text{wall}}, \quad (20)$$

where  $\Gamma_D^{\text{in}} = [0, 1] \times \{1\}$  and  $\Gamma_D^{\text{wall}} = \partial\Omega \setminus \Gamma_D^{\text{in}}$ . For the corresponding macroscale model (4)–(10), we impose the following conditions on the external boundary of the coupled domain

$$\bar{\mathbf{v}} = (1, 0) \text{ on } \Gamma_D^{\text{in}}, \quad \bar{\mathbf{v}} = \mathbf{0} \text{ on } \Gamma_{D,\text{ff}}^{\text{wall}}, \quad \bar{v} = 0 \text{ on } \Gamma_{N,\text{pm}}^{\text{wall}}, \quad (21)$$

where  $\Gamma_{D,\text{ff}}^{\text{wall}} = \Gamma_D^{\text{wall}} \cap \partial\Omega_{\text{ff}}$  and  $\Gamma_{N,\text{pm}}^{\text{wall}} = \Gamma_D^{\text{wall}} \cap \partial\Omega_{\text{pm}}$ . Since the flow is almost parallel to the porous bed (fig. 9, left), we consider the same upper boundary  $M = 10$  for the Beavers–Joseph slip coefficient for the minimization approach presented in section 3.2.

In fig. 9, we present the pore-scale velocity magnitude (left) and the tangential velocity profiles at  $x_1 = 0.5$  (right). The optimal values of  $\alpha_{\text{BJ}}$  are provided in table 3 for two different cross sections: at  $x_1 = 0.1$ , where the flow is not completely parallel to the porous bed, and in the middle of the domain at  $x_1 = 0.5$ , where the flow is parallel to the interface. For the first cross section, we obtained the same optimal value of the Beavers–Joseph slip coefficient  $\alpha_{\text{BJ}}^{\text{opt}} = 0.3$  for both velocity components. In the middle of the domain, the normal component of velocity  $v_2$  is zero. Therefore, at this cross section, the contribution of  $v_2$  is irrelevant for the determination of the optimal value  $\alpha_{\text{BJ}}^{\text{opt}}$  as in the case for the pressure-driven flow in section 4.1 due to zero errors (table 3). The optimal values of the Beavers–Joseph parameter are slightly different for the two considered cross sections due to different flow directions at the fluid–porous interface.

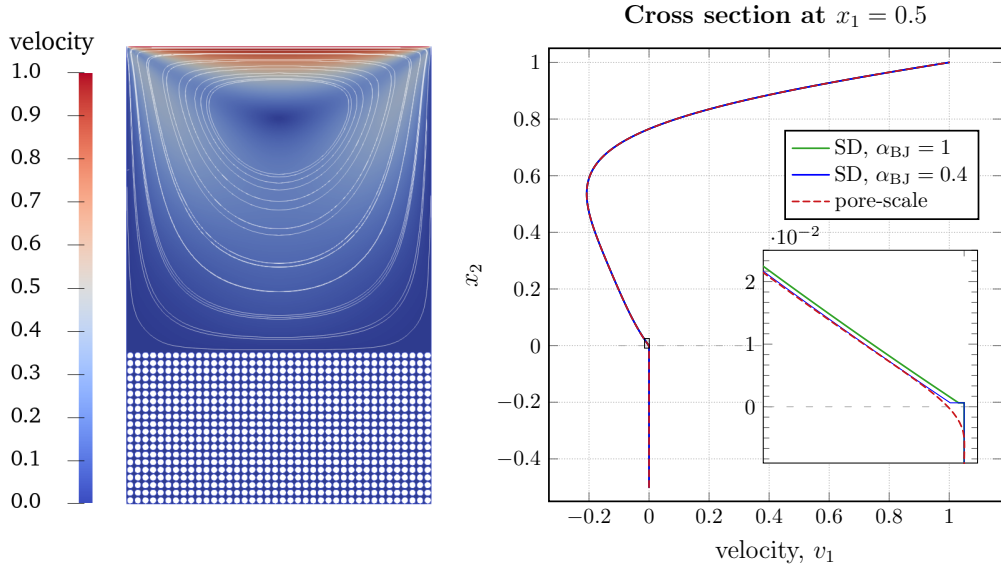


Figure 9: Microscale velocity field (left) and tangential velocity profiles (right) for the lid-driven cavity over porous bed with geometry  $G_2$  and  $\varepsilon = 1/40$ .

Note that in [29] the value  $\alpha_{\text{BJ}} = 0.5$  was found to be a better choice than  $\alpha_{\text{BJ}} = 1$  considering exactly the same flow problem and the same pore

geometry. However, in [29] the optimal value of the Beavers–Joseph slip coefficient was not computed, but only estimated.

Cross section	Velocity	$\alpha_{\text{BJ}}^{\text{opt}}$	Error for $\alpha_{\text{BJ}}^{\text{opt}}$	Error for $\alpha_{\text{BJ}} = 1$
$x_1 = 0.1$	$v_1$	0.3	0.000130	0.000189
$x_1 = 0.1$	$v_2$	0.3	0.000102	0.000425
$x_1 = 0.5$	$v_1$	0.4	0.000237	0.000688
$x_1 = 0.5$	$v_2$	–	0	0

Table 3: Optimal Beavers–Joseph parameters  $\alpha_{\text{BJ}}^{\text{opt}}$  and relative errors between the pore-scale and macroscale simulation results  $\epsilon_{v_i, x_1}$ ,  $i = 1, 2$  given in (17) for the lid-driven cavity over porous bed and  $G_2$  with  $\epsilon = 1/40$ .

### 4.3. General filtration problem

In order to show that the Beavers–Joseph condition is not applicable for multidimensional flows to the fluid–porous interface, we study a general filtration problem, where the flow is arbitrary to the porous bed. We consider the free-flow region  $\Omega_{\text{ff}} = [0, 1] \times [0, 0.5]$ , the interface  $\Gamma = [0, 1] \times \{0\}$  and the porous medium  $\Omega_{\text{pm}} = [0, 1] \times [-0.5, 0]$ , which includes  $20 \times 10$  circular solid grains ( $\epsilon = 1/20$ ) with radius  $r = 0.25\epsilon$  (geometry  $G_1$ ).

For the pore-scale problem (1)–(3), we impose the following boundary conditions to obtain an arbitrary flow to the porous layer (fig. 10, left):

$$\begin{aligned} \bar{\mathbf{v}} &= (0, -0.7 \sin(\pi x_1)) \quad \text{on } \Gamma_D^{\text{in}}, & \bar{\mathbf{v}} &= \mathbf{0} \quad \text{on } \Gamma_D^{\text{wall}}, \\ \bar{\mathbf{h}} \cdot \mathbf{n} &= 0 \quad \text{on } \Gamma^{\text{out}}, & \bar{\mathbf{v}} \cdot \boldsymbol{\tau} &= 0 \quad \text{on } \Gamma^{\text{out}}, \end{aligned} \quad (22)$$

where  $\Gamma_D^{\text{in}} = [0, 1] \times \{0.5\}$ ,  $\Gamma^{\text{out}} = (\{0\} \times (0, 0.5)) \cup (\{1\} \times (0, 0.225))$ , and  $\Gamma_D^{\text{wall}} = \partial\Omega \setminus (\Gamma_D^{\text{in}} \cup \Gamma^{\text{out}})$ .

The macroscale model (4)–(10) is complemented by the following boundary conditions

$$\begin{aligned} \bar{\mathbf{v}} &= (0, -0.7 \sin(\pi x_1)) \quad \text{on } \Gamma_D^{\text{in}}, & \bar{\mathbf{v}} &= \mathbf{0} \quad \text{on } \Gamma_{D, \text{ff}}^{\text{wall}}, \\ \bar{\mathbf{h}} \cdot \mathbf{n} &= 0, \quad \bar{\mathbf{v}} \cdot \boldsymbol{\tau} = 0 \quad \text{on } \Gamma^{\text{out}}, & \bar{v} &= 0 \quad \text{on } \Gamma_{N, \text{pm}}^{\text{wall}}, \end{aligned} \quad (23)$$

where  $\Gamma_{D, \text{ff}}^{\text{wall}} = \Gamma_D^{\text{wall}} \cap \partial\Omega_{\text{ff}}$  and  $\Gamma_{N, \text{pm}}^{\text{wall}} = \Gamma_D^{\text{wall}} \cap \partial\Omega_{\text{pm}}$ .

In fig. 10 (left), we present the pore-scale velocity field for the general filtration problem with arbitrary flow direction to the porous layer. Since the

flow is non-parallel to the fluid–porous interface in this case, we consider a broader range of the Beavers–Joseph parameters setting the upper boundary  $M = 100$  for the minimization procedure proposed in section 3.2.

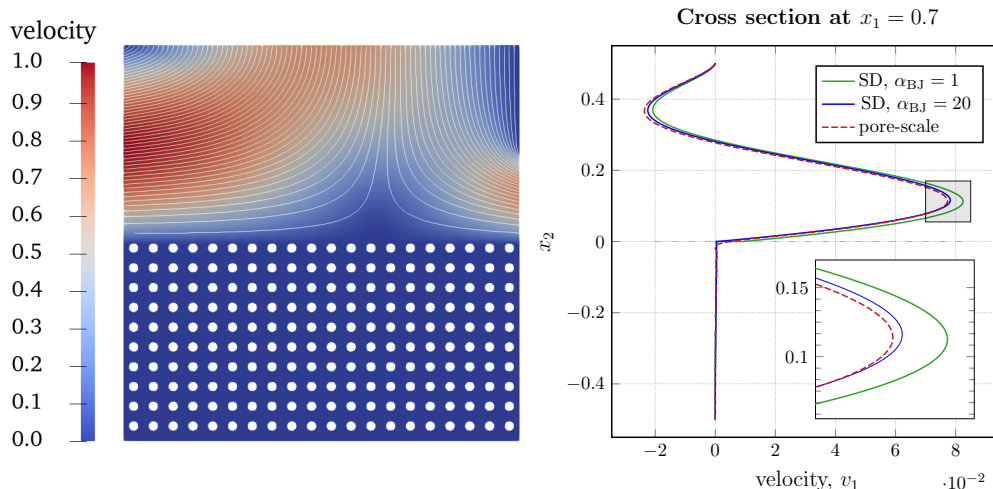


Figure 10: Microscale velocity field (left) and tangential velocity profiles (right) for the general filtration problem with geometry  $G_1$  and  $\varepsilon = 1/20$ .

In fig. 10 (right), we provide the pore-scale resolved and macroscale velocity profiles for the tangential component at  $x_1 = 0.7$ . The macroscale tangential velocity profile with the typically used value  $\alpha_{BJ} = 1$  does not fit to the pore-scale resolved model. The difference between the macroscale simulation results and the pore-scale resolved model given by (17) for the tangential velocity  $v_1$  is becoming smaller for bigger values of the Beavers–Joseph slip coefficient  $\alpha_{BJ}$ . However, these improvements are minor for  $\alpha_{BJ} \in [20, 100]$ . Therefore, we can take  $\alpha_{BJ}^{\text{opt}} = 20$  at  $x_1 = 0.7$  for the tangential velocity. As can be seen from fig. 10 (right), the macroscale profile with the Beavers–Joseph slip coefficient  $\alpha_{BJ} = 20$  fits much better to the pore-scale resolved model.

We consider four different cross sections and provide the optimal values  $\alpha_{BJ}^{\text{opt}}$  and the errors (17) for both velocity components in table 4. We observe that the optimal value of Beavers–Joseph parameter is different for every cross section and each velocity component. Therefore, in case of arbitrary flow direction to the fluid–porous interface, the Beavers–Joseph slip coefficient  $\alpha_{BJ}$  is not constant along the interface and the optimal value cannot be found globally.

Cross section	Velocity	$\alpha_{\text{BJ}}^{\text{opt}}$	Error for $\alpha_{\text{BJ}}^{\text{opt}}$	Error for $\alpha_{\text{BJ}} = 1$
$x_1 = 0.5$	$v_1$	5.0	0.006620	0.024840
$x_1 = 0.5$	$v_2$	3.9	0.001283	0.008858
$x_1 = 0.7$	$v_1$	20.0	0.034675	0.099011
$x_1 = 0.7$	$v_2$	3.3	0.001638	0.010869
$x_1 = 0.8$	$v_1$	3.7	0.015099	0.040387
$x_1 = 0.8$	$v_2$	4.1	0.001691	0.011077
$x_1 = 0.9$	$v_1$	3.2	0.012151	0.035285
$x_1 = 0.9$	$v_2$	3.6	0.004638	0.009416

Table 4: Optimal Beavers–Joseph parameters  $\alpha_{\text{BJ}}^{\text{opt}}$  and relative errors between the pore-scale and macroscale simulation results  $\epsilon_{v_i, x_1}$ ,  $i = 1, 2$  given in (17) for the general filtration problem and  $G_1$  with  $\varepsilon = 1/20$ .

## 5. Discussion

In this paper, we analyzed the applicability of the Beavers–Joseph interface condition (10) to different flow problems and studied the dependency of the Beavers–Joseph slip coefficient  $\alpha_{\text{BJ}}$  on the flow regime, the pore geometry, the permeability, the porosity and the pore-scale surface roughness. We found out that (i) the Beavers–Joseph parameter is in general not constant along the fluid–porous interface; (ii) its value  $\alpha_{\text{BJ}} = 1$  typically used in the literature is not correct for many flow problems; (iii) the optimal value of the Beavers–Joseph slip coefficient can be found only for unidirectional flows; (iv) the slip coefficient depends on the pore-scale geometrical information including the microscale surface roughness, but is independent of the velocity magnitude for parallel flows.

These conclusions are made based on the detailed study of three different flow problems: 1) the pressure-driven flow with unidirectional fluid flow parallel to the fluid–porous interface; 2) the lid-driven cavity over porous bed, where the fluid flow is almost parallel to the porous layer; and 3) the general filtration problem, where the flow direction is arbitrary. We analyzed different types of porous media: isotropic, orthotropic, and anisotropic. To find the optimal value of the Beavers–Joseph parameter  $\alpha_{\text{BJ}}$  we minimize the error between the macroscale solution of the Stokes/Darcy problem and the pore-scale resolved model. The Clough–Tocher interpolation is used to deal with two different computational grids and the minimization procedure is based on simulated annealing. The effective permeability for the coupled

macroscale Stokes/Darcy problem is computed numerically using the theory of homogenization. In order to study the dependency of the optimal Beavers–Joseph parameter on the pore geometry, we constructed porous media having the same effective properties (porosity, permeability) but different porous structures (circular and squared solid grains). To analyze the dependency of  $\alpha_{\text{BJ}}$  on the interface roughness, we considered different configurations of the porous bed having the same surface roughness. We studied different velocity magnitudes and flow directions for the same geometrical configurations to investigate the impact of the free flow on the overall system behavior. We also confirmed the result from [29], where  $\alpha_{\text{BJ}} = 1$  was found to be not the best choice for the lid-driven cavity over porous bed considering the same flow problem and optimizing the Beavers–Joseph slip coefficient.

To summarize, the Beavers–Joseph condition is not applicable to general flow problems in coupled systems with arbitrary flow directions to the fluid–porous interface. However, for parallel or almost parallel flows to the porous medium, the Beavers–Joseph slip coefficient can be determined using pore-scale information such that it provides accurate simulation results for the macroscale Stokes/Darcy problem. For the case of arbitrary flows, alternative sets of interface conditions should be used, e.g. those proposed in [4] or [21].

## Acknowledgments

The work is funded by the Deutsche Forschungsgemeinschaft (DFG, German Research Foundation) – Project Number 327154368 – SFB 1313.

## References

- [1] L. Beaudé, K. Brenner, S. Lopez, R. Masson, F. Smai, Non-isothermal compositional liquid gas Darcy flow: formulation, soil-atmosphere boundary condition and application to high-energy geothermal simulations, *Comput. Geosci.* 23 (2019) 443–470. doi:10.1007/s10596-018-9794-9.
- [2] F. Cimolin, M. Discacciati, Navier–Stokes/Forchheimer models for filtration through porous media, *Appl. Numer. Math.* 72 (2013) 205–224. doi:10.1016/j.apnum.2013.07.001.



- [3] B. Reuter, A. Rupp, V. Aizinger, P. Knabner, Discontinuous Galerkin method for coupling hydrostatic free surface flows to saturated subsurface systems, *Comput. Math. Appl.* 77 (2019) 2291–2309. doi:10.1016/j.camwa.2018.12.020.
- [4] P. Angot, B. Goyeau, J. A. Ochoa-Tapia, Asymptotic modeling of transport phenomena at the interface between a fluid and a porous layer: jump conditions, *Phys. Rev. E* 95 (6) (2017) 063302. doi:10.1103/PhysRevE.95.063302.
- [5] M. Discacciati, E. Miglio, A. Quarteroni, Mathematical and numerical models for coupling surface and groundwater flows, *Appl. Num. Math.* 43 (2002) 57–74. doi:10.1016/S0168-9274(02)00125-3.
- [6] W. Jäger, A. Mikelić, Modeling effective interface laws for transport phenomena between an unconfined fluid and a porous medium using homogenization, *Transp. Porous Med.* 78 (2009) 489–508. doi:10.1007/s11242-009-9354-9.
- [7] U. Lācis, S. Bagheri, A framework for computing effective boundary conditions at the interface between free fluid and a porous medium, *J. Fluid Mech.* 812 (2017) 866–889. doi:10.1017/jfm.2016.838.
- [8] G. S. Beavers, D. D. Joseph, Boundary conditions at a naturally permeable wall, *J. Fluid Mech.* 30 (1967) 197–207. doi:10.1017/S0022112067001375.
- [9] C. Dawson, A continuous/discontinuous Galerkin framework for modeling coupled subsurface and surface water flow, *Comput. Geosci.* 12 (2008) 451–472. doi:10.1007/s10596-008-9085-y.
- [10] T. Carraro, C. Goll, A. Marciniak-Czochra, A. Mikelić, Effective interface conditions for the forced infiltration of a viscous fluid into a porous medium using homogenization, *Comput. Methods Appl. Mech. Engrg.* 292 (2015) 195–220. doi:10.1016/j.cma.2014.10.050.
- [11] P. Sochala, A. Ern, S. Piperno, Mass conservative BDF-discontinuous Galerkin/explicit finite volume schemes for coupling subsurface and overland flows, *Comput. Methods Appl. Mech. Engrg.* 198 (2009) 2122–2136. doi:10.1016/j.cma.2009.02.024.

- [12] E. Eggenweiler, I. Rybak, Unsuitability of the Beavers–Joseph interface condition for filtration problems, *J. Fluid Mech.* 892 (2020) A10. doi:10.1017/jfm.2020.194.
- [13] M. Discacciati, A. Quarteroni, Navier–Stokes/Darcy coupling: modeling, analysis, and numerical approximation, *Rev. Mat. Complut.* 22 (2009) 315–426. doi:10.5209/rev\REMA.2009.v22.n2.16263.
- [14] J. Magiera, C. Rohde, I. Rybak, A hyperbolic-elliptic model problem for coupled surface-subsurface flow, *Transp. Porous Med.* 114 (2016) 425–455. doi:10.1007/s11242-015-0548-z.
- [15] K. Mosthaf, K. Baber, B. Flemisch, R. Helmig, A. Leijnse, I. Rybak, B. Wohlmuth, A coupling concept for two-phase compositional porous-medium and single-phase compositional free flow, *Water Resour. Res.* 47 (2011) W10522. doi:10.1029/2011WR010685.
- [16] I. Rybak, J. Magiera, R. Helmig, C. Rohde, Multirate time integration for coupled saturated/unsaturated porous medium and free flow systems, *Comput. Geosci.* 19 (2015) 299–309. doi:10.1007/s10596-015-9469-8.
- [17] M. Amara, D. Capatina, L. Lizaik, Coupling of Darcy–Forchheimer and compressible Navier–Stokes equations with heat transfer, *SIAM J. Sci. Comput.* 31 (2009) 1470–1499. doi:10.1137/070709517.
- [18] K. Alazmi, B. Vafai, Analysis of fluid flow and heat transfer interfacial conditions between a porous medium and a fluid layer, *Int. J. Heat Mass Transfer* 44 (2001) 1735–1749. doi:10.1016/S0017-9310(00)00217-9.
- [19] P. Angot, B. Goyeau, J. Ochoa-Tapia, A nonlinear asymptotic model for the inertial flow at a fluid-porous interface, *Adv. Water Res.* 149 (2021) 103798. doi:10.1016/j.advwatres.2020.103798.
- [20] W. Jäger, A. Mikelić, On the interface boundary conditions by Beavers, Joseph and Saffman, *SIAM J. Appl. Math.* 60 (2000) 1111–1127. doi:10.1137/S003613999833678X.
- [21] E. Eggenweiler, I. Rybak, Effective coupling conditions for arbitrary flows in Stokes–Darcy systems, *Multiscale Model. Simul.* 19 (2021) 731–757. doi:10.1137/20M1346638.

- [22] A. J. Ochoa-Tapia, S. Whitaker, Momentum transfer at the boundary between a porous medium and a homogeneous fluid. I: Theoretical development, *Int. J. Heat Mass Transfer* 38 (1995) 2635–2646. doi:10.1016/0017-9310(94)00347-X.
- [23] P. G. Saffman, On the boundary condition at the surface of a porous medium, *Stud. Appl. Math.* 50 (1971) 93–101. doi:10.1002/sapm197150293.
- [24] I. P. Jones, Low Reynolds number flow past a porous spherical shell, *Proc. Camb. Phil. Soc.* 73 (1973) 231–238. doi:10.1017/S0305004100047642.
- [25] N. S. Hanspal, A. N. Waghode, V. Nassehi, R. J. Wakeman, Numerical analysis of coupled Stokes/Darcy flows in industrial filtrations, *Transp. Porous Med.* 64 (2006) 383–411. doi:10.1007/s11242-005-1457-3.
- [26] M. Discacciati, L. Gerardo-Giorda, Optimized Schwarz methods for the Stokes–Darcy coupling, *IMA J. Numer. Anal.* 38 (2018) 1959–1983. doi:10.1093/imanum/drx054.
- [27] M. Mierzwiczak, A. Fraska, J. Grabski, Determination of the slip constant in the Beavers–Joseph experiment for laminar fluid flow through porous media using a meshless method, *Math. Probl. Eng.* 2019, Article ID 1494215 (2019). doi:10.1155/2019/1494215.
- [28] G. Yang, E. Coltman, K. Weishaupt, A. Terzis, R. Helmig, B. Weigand, On the Beavers–Joseph interface condition for non-parallel coupled channel flow over a porous structure at high Reynolds numbers, *Transp. Porous Med.* 128 (2019) 431–457. doi:10.1007/s11242-019-01255-5.
- [29] I. Rybak, C. Schwarzmeier, E. Eggenweiler, U. Rüde, Validation and calibration of coupled porous-medium and free-flow problems using pore-scale resolved models, *Comput. Geosci.* 25 (2021) 621–635. doi:10.1007/s10596-020-09994-x.
- [30] A. Terzis, I. Zarikos, K. Weishaupt, G. Yang, X. Chu, R. Helmig, B. Weigand, Microscopic velocity field measurements inside a regular porous medium adjacent to a low Reynolds number channel flow, *Phys. Fluids* 31 (2019) 042001. doi:10.1063/1.5092169.

- [31] U. Lācis, Y. Sudhakar, S. Pasche, S. Bagheri, Transfer of mass and momentum at rough and porous surfaces, *J. Fluid Mech.* 884 (2020) A21. doi:10.1017/jfm.2019.897.
- [32] U. Hornung, *Homogenization and Porous Media*, Springer-Verlag, New York, 1997.
- [33] P. Alfeld, A trivariate Clough–Tocher scheme for tetrahedral data, *Comput. Aided Geom. Design* 1 (1984) 169–181. doi:10.1016/0167-8396(84)90029-3.
- [34] G. M. Nielson, A method for interpolating scattered data based upon a minimum norm network, *Math. Comp.* 40 (1983) 253–217. doi:10.2307/2007373.
- [35] F. Hecht, New development in FREEFEM++, *J. Numer. Math.* 20 (2012) 251–265. doi:10.1515/jnum-2012-0013.
- [36] W. J. Layton, F. Schieweck, I. Yotov, Coupling fluid flow with porous media flow, *SIAM J. Numer. Anal.* 40 (2003) 2195–2218. doi:10.1137/S0036142901392766.